COVID

MDPI

Article

In Silico Evaluation of Potential SARS-CoV-2 RNA-Dependent RNA Polymerase (RdRp) Inhibitors Derived from Philippine Natural Products

Alexandra Isabelle D. Ang [1], Alexandra P. Lee [1], Junie B. Billones [1], Lyre Anni E. Murao [2], Maria Constancia O. Carrillo [1] and Stephani Joy Y. Macalino [3,*]

[1] Department of Physical Sciences and Mathematics, College of Arts and Sciences, University of the Philippines Manila, Manila 1000, Philippines; adang3@up.edu.ph (A.I.D.A.); aplee2@up.edu.ph (A.P.L.); jbbillones@up.edu.ph (J.B.B.); mtobrerocarrillo@up.edu.ph (M.C.O.C.)
[2] Department of Biological Science and Environmental Studies, College of Science and Mathematics, University of the Philippines Mindanao, Davao 8000, Philippines; lemurao@up.edu.ph
[3] Department of Chemistry, College of Science, De La Salle University, Manila 0922, Philippines
* Correspondence: stephani.macalino@dlsu.edu.ph

Abstract

RNA-dependent RNA-polymerase (RdRp), one of the key enzymes in the Severe Acute Respiratory Syndrome Coronavirus 2 (SARS-CoV-2) life cycle, is a recognized druggable target for Coronavirus disease 19 (COVID-19) treatment. Its inhibition has been associated with reduced viral loads in infected individuals. A library of 1562 Philippine Natural Compounds was screened in silico for potential SARS-CoV-2 anti-RdRp activity using a high-throughput virtual screening (VS) approach. Molecular docking experiments and in silico absorption, distribution, metabolism, and excretion (ADME) predictions were used to determine compounds with potential inhibitory capabilities against RdRp. The top three compounds, Vitelignin A (VIT), Vitexoside (VIX), and Cannabifolin C (CAN), were subjected to molecular dynamics (MD) simulations in complex with RdRp, confirming the formation of stable protein-ligand complexes. Overall, these results suggest promising inhibitory capabilities of these three compounds against SARS-CoV-2 RdRp. Their shared presence in extracts of *Vitex negundo*, a Philippine medicinal plant, warrants further in vitro and in vivo investigation regarding the anti-SARS-CoV-2 activity of its extracts and active components.

Keywords: SARS-CoV-2; RNA-Dependent RNA Polymerase; in silico drug discovery; virtual screening; molecular dynamics

Academic Editors: Martin Kröger and Reinhard Schlickeiser

Received: 11 January 2026
Revised: 8 July 2026
Accepted: 15 July 2026
Published: 20 July 2026

1. Introduction

Coronavirus disease 19 (COVID-19) is a pathogenic viral infection caused by Severe Acute Respiratory Syndrome Coronavirus 2 (SARS-CoV-2) [1]. Cases of this viral infection were first reported in December 2019 in Wuhan, Hubei Province, China, but eventually quickly spread worldwide [2,3]. As of July 2024, a total of 775,830,200 cases and 7,056,108 deaths were reported worldwide. In the Philippines, a total of 4,140,383 cases have been reported, with 66,864 deaths [4]. Increased mortality for COVID-19 compared to previous coronavirus outbreaks was attributed to mutations in the SARS-CoV-2 viral genome, which increased the transmissibility of the virus [5].

SARS-CoV-2 is a positive-sense, single-stranded RNA virus belonging to the beta genus of the coronavirus family [6]. These diverse viruses feature four characteristic

structural proteins: spike (S), envelope (E), membrane (M), and nucleocapsid (N). Of these, the S protein notably mediates virion attachment and envelope fusion with the host cell [7]. When the virus has infiltrated the host cell, the next order of action is to express and replicate its genetic material to continue infection. Positive-strand RNA viruses like SARS-CoV-2 contain message-sense genomes, which can be used as direct templates for the creation of viral particles and other nonstructural polyproteins [8]. Knowledge of the mechanism of SARS-CoV-2 invasion in the host provides insight into additional points of intervention that may be exploited for therapy.

RNA-dependent RNA polymerase (RdRp) is one of the nonstructural proteins (nsp) coded by the SARS-CoV-2 virus [9]. RdRp adopts a three-dimensional structure that is described to have right-handed architecture with fingers, palm, and thumb subdomains. In SARS-CoV-2, RdRp is designated as nsp12 and facilitates viral RNA synthesis in the host cell. Specifically, this enzyme is solely tasked with reading RNA templates and catalyzing phosphodiester bond formation between nucleoside triphosphates (NTPs). RdRp, however, does not act alone; it usually forms multi-subunit polymerase complexes with other proteins that aid in regulating and coordinating relevant RNA processes to the viral life cycle [8]. Because RdRp is a key component in the COVID-19 replication-transcription complex, it is an attractive enzyme to target for antiviral treatment. Furthermore, its high conservation across various RNA virus families has made this protein a focus of drug discovery screens for broad-spectrum therapeutics against multiple pathogens.

This paper reports *Vitex negundo* as a potential source of SARS-CoV-2 inhibitors. *Vitex negundo* is a plant that is widely distributed across Asia and some parts of Africa, and has long been used as a traditional medicine in the Philippines for various respiratory problems. The identification of compounds from this plant that can potentially target SARS-CoV-2 RdRp presents another appealing benefit for this commonly used herbal medicine.

In silico approaches, specifically predictive ADME screening, molecular docking, and molecular dynamics (MD), were used to assess the binding affinity of potential inhibitors against SARS-CoV-2 RdRp. Utilizing in silico compound screening provides a method to streamline the testing process by predicting the safety and druggability of potential candidates and initially identifying compounds that may be received well by the target enzyme, RNA-dependent RNA polymerase, from a large pool of compounds before in vitro validation or in vivo trials. Compounds identified with inhibitory properties from this study may then be used as a basis for future studies to validate and test the identified compounds through in vitro screening for the SARS-CoV-2 virus.

2. Materials and Methods

2.1. Initial Molecular Dynamics Simulation and Clustering of Apo RdRp Structure

The target enzyme for this study was the RNA-dependent RNA polymerase of SARS-CoV-2. The structure of SARS-CoV-2 RdRp in complex with its cofactors nsp7 and nsp8 was obtained from the CHARMM-GUI Archive–COVID-19 Proteins Library for use in the MD and docking steps [10]. This structure completes the residues that were left unresolved in the RdRp complex structure submitted to the Research Collaboratory for Structural Bioinformatics Protein Data Bank (RCSB PDB) with the PDB ID: 6M71 [1]. Protein chains from this structure were re-labeled according to designations in the original RCSB PDB file.

To optimize the structure of RNA-dependent RNA-polymerase for the chosen system, the protein structure obtained from the CHARMM-GUI Archive was refined through MD using GROMACS 2023 [11,12]. Protein topology was generated, applying the CHARMM27 all-atom force field for the calculations [13]. The enzyme complex was then enclosed in a simple cubic box 1.0 nm away from the protein edge and solvated with TIP3P water molecule models. Na^+/Cl^- counterions were added to neutralize the established system.

The final apo protein system had an approximate size of 138 × 138 × 138 Å and was composed of a 1135 residue protein complex, 12 sodium ions, and 79,602 water molecules. The established system was then subjected to energy minimization, applying the steepest descent minimization algorithm to converge energies to 1000 kJ/mol using a maximum of 50,000 descent steps with a 0.01 nm step size. This was then equilibrated using two consecutive steps involving (1) a canonical (NVT) ensemble and (2) an isothermal-isobaric (NPT) ensemble. In the NVT ensemble, the system was stabilized to 300 K using the Nosé–Hoover thermostat [14,15]. The NPT ensemble was equilibrated using the Parrinello–Rahman barostat [16] to establish a system with an average pressure close to 1 bar. Both equilibration steps were performed with a 1 fs time step for 1 ns each. After equilibration, a production run of 100 ns with a time step of 1 fs was executed. The system was kept at 300 K and 1 bar using the Nosé–Hoover thermostat and Parrinello–Rahman barostat, respectively. Non-bonded interactions were established with a cut-off value of 1.2 nm and switching distance of 1.0 nm, while electrostatic interactions were set using Particle Mesh Ewald (PME) calculations with a 1.2 nm cut-off. Hydrogen bond constraints were also employed using the LINear Constraint Solver (LINCS) algorithm. After the production run, the periodic boundary conditions of the system were fixed.

Trajectory analysis for the MD run was performed to obtain the Root Mean Square Deviation (RMSD), Root Mean Square Fluctuation (RMSF), and Radius of Gyration (ROG). The GROMACS cluster function was used to generate clustered structures from the simulation using the gromos method and with a cutoff of 0.2 nm. A representative structure from the most populated cluster was selected for the molecular docking of Philippine natural product compounds.

2.2. Virtual Screening

The structure for the control ligand, Remdesivir Triphosphate (RTP), was retrieved from PubChem (https://pubchem.ncbi.nlm.nih.gov, 24 May 2021) in SDF format. An in-house compound library of 1562 Philippine Natural Products was also acquired for the virtual screening (unpublished). The molecules were configured and prepared for docking using Open Babel 3.1.1 [17]. Each compound was converted to a pdbqt file format and minimized using the Merck Molecular Force Field 94 (MMFF94). To prepare the protein structure for docking, AutoDock Tools 1.5.6 was used to add polar hydrogens and Kollman charges to the protein complex [18,19].

Molecular docking simulations were then performed using the clustered apo protein structure from the previous MD step. A grid box enclosing previously identified active-site residues of the RdRp catalytic domain (Table 1) was created for the docking of both the control and the Philippine Natural Products compounds library. The configuration box used throughout the docking procedure was 25 × 32 × 38 Å in size and centered around critical residues in the catalytic subunit located at xyz coordinates (−6.776, −5.882, 4.426). Each compound was docked with exhaustiveness set to 24, energy range of 4, and num mode equal to 30 using AutoDock Vina [20].

Table 1. Summary of SARS-CoV-2 RdRp active-site residues noted in the previous literature.

Motif A [N611–P627]	Motif B [G678–T710]	Motif C [F753–N767]	Motif D [L775–E795]	Motif E [H810–K821]	Motif F [L544–V557]	Motif G [D499–L514]	Other Residues	Ref.
D618		S759 D760 D761			K545 R553 R555			[1]

Table 1. *Cont.*

Motif A [N611–P627]	Motif B [G678–T710]	Motif C [F753–N767]	Motif D [L775–E795]	Motif E [H810–K821]	Motif F [L544–V557]	Motif G [D499–L514]	Other Residues	Ref.
					K545 R555			[21]
D623	S682 N691	S759 D760 D761						[22]
G616 W617 D618 Y619		L758 S759 D760 D761 A762		E811 F812 C813 S814			K798 C799 W800	[9]

Ligands were first screened based on binding affinity, where molecules with binding affinities more positive than RTP were immediately excluded. The top 25% of the remaining ligands were visually assessed through Pymol 2.4.1 [23] and assigned clusters (RMSD < 2.0 Å). With this, the conformation from the most populated group with the best binding affinity was chosen, isolated, and converted to PDB format. These conformations were used to re-rank the docking results. The remaining ligands were screened for their ADME properties through the SwissADME server [24]. Although it is important to note that these predictions still has to be validated in the laboratory to study for potential toxicity and adverse effects, metabolism of the compounds that might lead to drug–drug interactions, and target specificity, in silico ADME provides a robust and quick means to predict the druggable properties of the candidates while also saving on resources as only the best compounds will be carried over for further experimental testing. Data for the selected ligand structures from clustering were then compiled in Microsoft Excel and sorted based on PAINS alert score, affinity, lipophilicity, and synthetic accessibility, respectively. Pharmacokinetic properties, such as CYP450 inhibition, P-gp binding, and predicted gastrointestinal absorption of the ligands, were also considered during the selection process, and hits with favorable properties were prioritized. The protein-ligand interactions of molecules that passed the affinity and ADME cutoffs were then inspected manually using Discovery Studio Visualizer 2021 [25]. The top ten hits were then selected based on ligand interactions with active and RNA interaction site residues. From this list, three structurally unique natural product compounds were selected for further analysis with MD.

2.3. Molecular Dynamics Simulation of Protein-Ligand Complexes

The top three Philippine natural product compounds, vitelignin A (VIT), vitexoside (VIX), and cannabifolin C (CAN), each complexed with the clustered apo RdRp structure from the initial simulation procedure, were each subjected to triplicate 100 ns MD simulations each. The respective protein topologies were first generated, applying the CHARMM27 all-atom force field for the calculations [13], after which the ligands were prepared for topology generation. Using Avogadro 1.2.0, hydrogens were added to the converted structures and saved as individual MOL2 files [26]. Ligand topologies were then generated using the SwissParam web server, which takes charges from the Merck Molecular Force Field and establishes van der Waals parameters from the CHARMM22 force field. Following this, the necessary configuration changes were made to the previously generated protein topology files [13,27]. The various RdRp-ligand complexes were then built from the prepared protein and ligand files taken from the docking experiments.

Following this, the protein-ligand complex systems were prepared using identical parameters as the apo RdRp system. Each of the three top hit-protein systems had an approximate size of 143 × 143 × 143 Å containing the 1135 residue RdRp protein complex, 1 natural product ligand, 12 sodium ions, and 89,525, 89,518, and 89,505 water molecules for the VIT, VIX, and CAN protein-ligand systems, respectively. All the systems were minimized, equilibrated, and run following the same specifications and steps as the apo RdRp MD simulation, except for the addition of protein-ligand coupling and independent protein and ligand position restraints.

Trajectory analysis for the MD run was performed to obtain the RMSD, RMSF, and ROG for the protein structures of the protein-ligand systems using the built-in calculations available in GROMACS. These were analyzed to obtain pertinent information on the stability of the system and any structural changes observed due to the presence of the added ligands. Additionally, hydrogen bond analysis was performed using VMD 1.9.4 [28] to observe prominent hydrogen bond interactions between the RdRp complex and the hits identified in this study. Furthermore, clustering was also performed using the same parameters as in the apo RdRp MD system to obtain and analyze the protein-ligand interactions for the representative structure of the most populated structure for each run.

3. Results

3.1. RdRp Apo Structure MD Simulation

MD simulation, as well as the measurement of structural parameters such as RMSD and RMSF, were used to assess the stability, dynamic behavior, and compactness of the functional RdRp complex prior to virtual screening. The calculated RMSD of the apo protein complex using C-alpha for the least-squares fit was found to plateau by the 30 ns mark, maintaining an average value of 6 and 5.5 Å with reference to the crystal and equilibrated structures, respectively (Figure 1a), indicating the overall stability of the resulting system after the MD simulation. RMSF value assessment for the RdRp subunits revealed that nsp12 maintained a relatively rigid conformation throughout the simulation in the polymerase N-terminal domain composed of the finger-palm-thumb subdomains (Figure 1b).

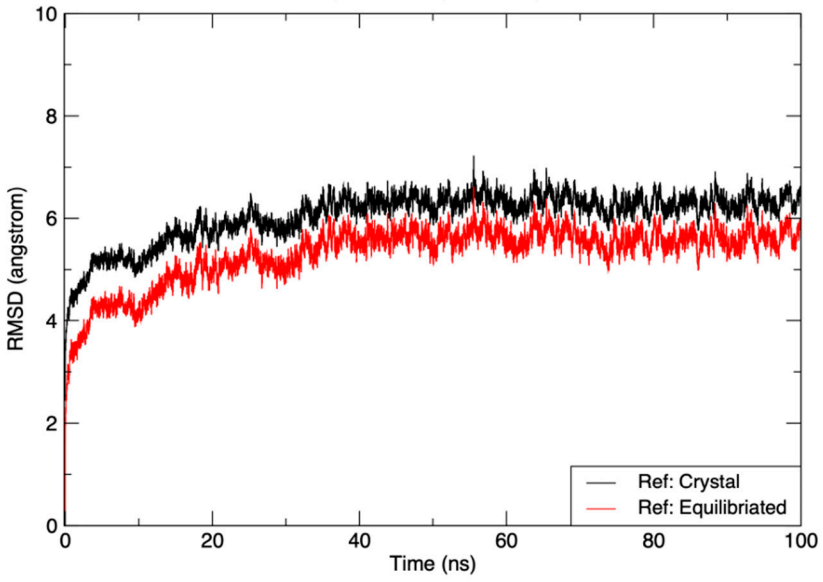

(a)

Figure 1. *Cont.*

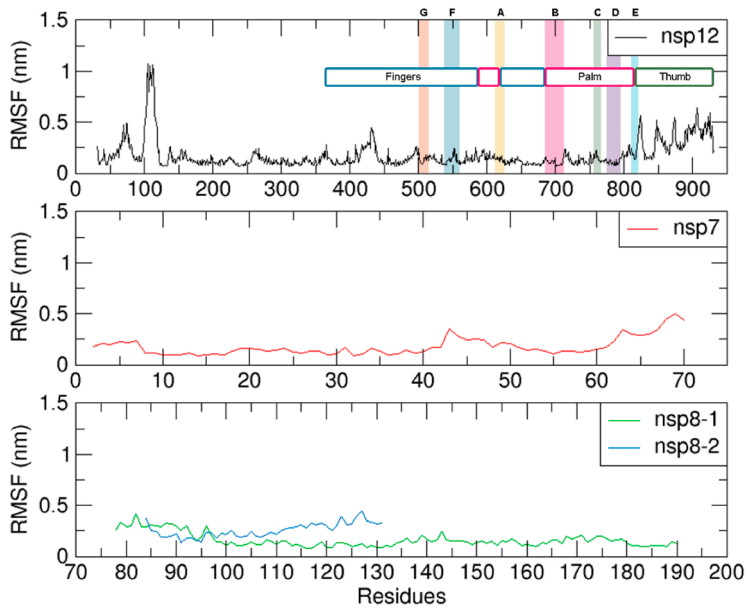

(**b**)

Figure 1. RdRp apo structure MD trajectory analysis. (**a**) RMSD based on C-alpha for the least-squares fit using the crystal (black) and equilibrated (red) structures as reference; (**b**) RMSF for the nsp12 (**top panel**), nsp7 (**middle panel**), and nsp8 (**bottom panel**) units of RdRp. Colored bars (top panel) highlight residues included in catalytic motifs A–G.

To obtain a structure that most accurately represents the RdRp complex and its most populated state during the simulation, trajectory frames from the MD simulation were clustered. When the clustered structure was superimposed on the pre-MD crystal structure, an RMSD value of 1.501 Å was obtained by comparing C-alpha positions, indicating that while differences are observed in local flexible regions of the protein, such as in the side chains and random loops, the overall backbone of RdRp still showed relative similarity between both structures, particularly in the active-site channels (Supplementary Figure S1). More evident conformational changes for the protein complex were observed in the thumb subdomain of the protein, Nidovirus RdRp-Associated Nucleotidyl transferase (NiRAN) region, and the other cofactors in the complex. Overall, these parameters indicate that the resulting protein structure was stable in the simulated system, and an optimized structure was successfully obtained for the following virtual screening protocol.

3.2. Virtual Screening of Philippine Natural Products

Molecular docking of RTP against the clustered apo RdRp resulted in a binding affinity of −7.9 kcal/mol. This value was then designated as the initial cut-off value for selecting potential hits from the in-house Philippine natural product compound library containing 1516 compounds. Upon docking, approximately one-fourth of the compounds from the library were found to have greater or equal binding affinities to RdRp compared to RTP. Cluster analysis was then performed on the top 25% of hits above the control cut-off (Supplementary Table S1) to identify compounds with relatively homogenous conformations and positions based on their docking position within the RdRp active site. This step minimized the possibility of selecting a pose that was not a representative solution during the search and identified favorable ligand binding regions within the protein search space. Further, these cluster 'hotspots' may also be associated with favorable entropic basins for protein conformation [29].

In silico ADME analysis was subsequently employed to predict the physicochemical properties that may highlight potential candidate drugs from the selected group of

compounds. To further narrow the search down to a smaller number of molecules, compounds were screened via SwissADME and filtered based on their lipophilicity (logP < 4) and various pharmacokinetic properties. Only compounds with Pan-Assay Interference Compounds (PAINS) values of zero, which predict decreased risk to false positive results in biochemical assays due to the presence of certain substructural motifs [30], were accepted for further consideration in anticipation of further in vitro assessment. Synthetic accessibility was also considered during screening to ensure that the natural product compound can be readily obtained by other methods if raw plant material is unavailable or not easily accessible. Applying these filters and prioritizing diversity in possible hit compounds, 10 Philippine natural products (Supplementary Tables S2 and S3) from the compound library were selected and further examined with respect to protein-ligand interactions. Interestingly, eight out of the ten compounds, namely Isocannabilignin, Cannabilignin, Vitexnegheteroin I, VIT, Vitegnoside, VIX, 6′-(p-hydroxybenzoyl)mussaenosidic acid, and CAN, were natural compounds isolated from various parts of the *Vitex negundo* plant, known more commonly in the Philippines as Lagundi [31–37].

3.3. Protein-Ligand Interactions and Selection of Top Hits

Compounds with the most interactions with critical residues within the RdRp binding site (Supplementary Figure S2) were selected for further processing and analysis using MD simulation. Critical residues were classified as either active-site (AS) or interaction site (IS) residues based on previous literature (Table 1). AS residues were those with noted involvement in the catalytic action of the protein and those that have been targeted in similar studies involving SARS-CoV-2 RdRp, while IS residues were assigned based on their function to stabilize the RNA template or primer strands during replication.

RTP (−7.9 kcal/mol) formed hydrogen bonds with R553, R555, S682, K621, R624, and E811. Notably, residues R553, R555, S682, and E811 were previously reported as active-site residues [1,9,21,22]. Pi-cation interactions were also observed with K621, R624, D760, D761, and E811. D760 and D761 represent catalytic domain residues conserved in other viruses [1,9,22]. van der Waals interactions were observed with Y619, P620, D623, T680, S681, T687, S759, F812, and S814. On the other hand, unfavorable interactions were recorded with Y456 and D760, potentially contributing to more unfavorable binding (Figure 2a,b; Table 2). The top-scored pose of VIT (−9.3 kcal/mol) was found to form hydrophobic contacts with V495, T565, R569, and A685 of SAR-CoV-2 RdRp. Hydrogen bonds with N497, S564, and R569 were also observed, all of which were residues part of the catalytic domain, despite not being noted in the previous literature. A pi-cation interaction with K500, a residue noted to accommodate RNA template strand binding, was also observed [21,22]. van der Waals interactions with N496, V557, A558, N568, G683, and D684 were also found between the protein and the compound (Figure 2c,d; Table 2). VIX (−8.8 kcal/mol) formed hydrophobic pi-alkyl contacts with K500, V557, and V560 in the docked complex. Hydrogen bonds were also formed with 6 residues, D452, N497, T556, G559, V560, and R624. The remaining interactions observed were from van der Waals contacts between VIX and residues V495, N496, S501, K545, R553, A554, R555, T565, K621, G683, A685, T687, S759, and D760. The ligand also showed unfavorable interactions with R624 and S682 (Figure 2e,f; Table 2). CAN (−8.3 kcal/mol) made hydrogen bond contacts with R553, E811, and S814 residues (Figure 2g,h; Table 2). van der Waals interactions between the protein and ligand were also observed with R555, D618, Y619, S759, D760, D761, H810, F812, and C813.

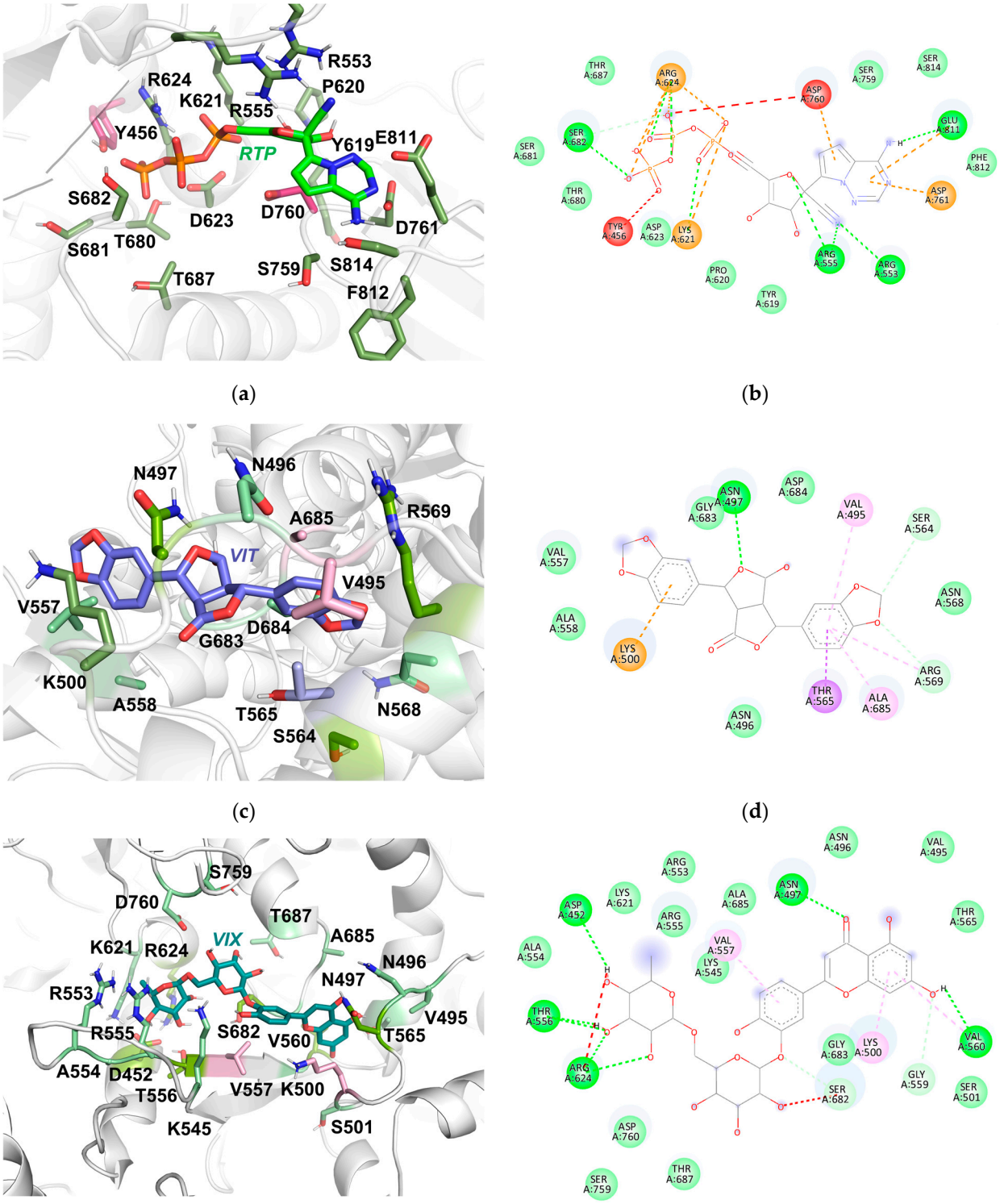

Figure 2. *Cont.*

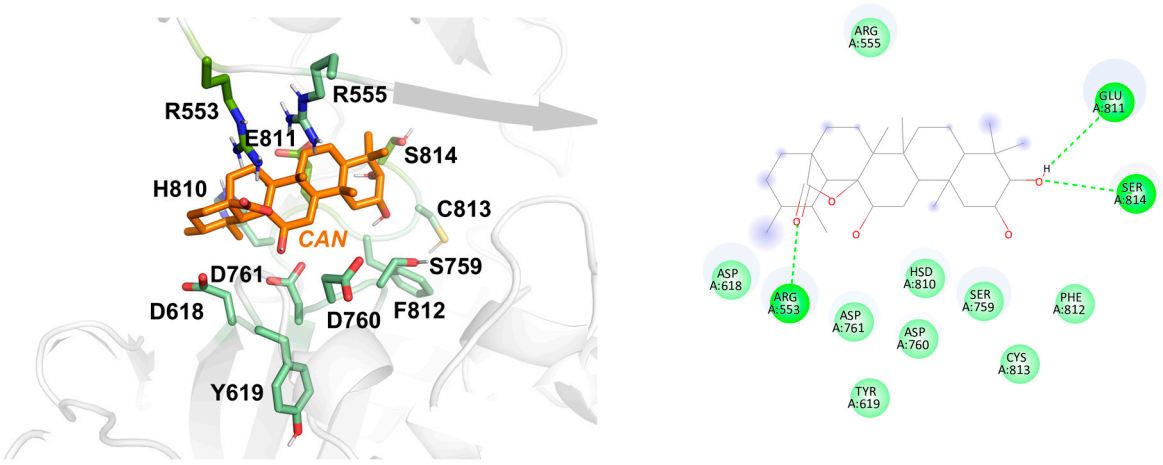

(**g**) (**h**)

Figure 2. Interaction diagrams from the selected conformation of RTP, VIT, VIX, and CAN docked against RNA-dependent RNA-polymerase in (**a**,**c**,**e**,**g**) 3D and (**b**,**d**,**f**,**h**) 2D representation, respectively. Hydrogen bonding is displayed as green dashed lines, van der Waals interactions are shown as green circles, and alkyl interactions are shown as pink circles. Unfavorable interactions are shown as red circles and red dashed lines, while charge and pi-charge interactions are shown as orange circles and orange dashed lines. Blue shadows on the ligand and residues indicate solvent accessibility.

Table 2. Summary of interactions observed for the top 3 compound-RdRp complexes after molecular docking.

Ligand	Hydrogen Bond	Hydrophobic	Charged	van der Waals
RTP	R553, R555, S682, K621, R624, E811	-	K621, R624, D760, D761, E811	Y619, P620, D623, T680, S681, T687, S759, F812, S814
VIT	N497, R569 [1], S564	V495, T565, R569 [1], A685	K500	N496, V557, A558, N568, G683, D684
VIX	D452, N497, T556, G559, V560, R624	K500, V557, V560	-	V495, N496, S501, K545, R553, A554, R555, T565, K621, G683, A685, T687, S759, D760
CAN	R553, E811, S814	-	-	R555, D618, Y619, S759, D760, D761, H810, F812, C813

[1] multiple interactions recorded.

With the information obtained from docking, ADME studies, and protein-ligand interaction analysis, VIT, VIX, and CAN (Figure 3), compounds derived from *Vitex negundo* were selected for further MD simulations and analysis.

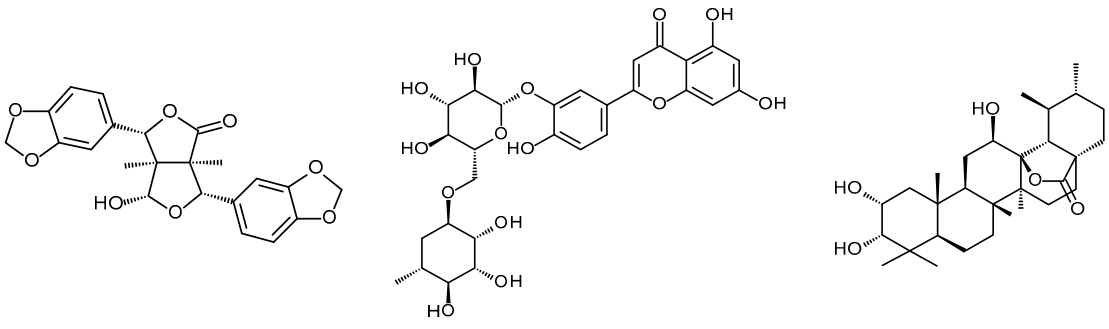

(**a**) (**b**) (**c**)

Figure 3. Two-dimensional Structures of the Top 3 Hit Compounds (**a**) VIT, (**b**) VIX, and (**c**) CAN.

3.4. Molecular Dynamics Simulations of Protein-Ligand Complexes

The previous molecular docking step examined protein-ligand interactions where the receptor, RdRp, and its cofactors were treated as static and only the ligands were flexible. This does not give the full perspective with respect to the dynamic movement the protein may exhibit when a ligand is bound to it. The application of MD allows protein-ligand or, in this case, drug-receptor interactions to be examined past the rigid lock-and-key paradigm [38]. Ligand interactions with the receptor may afford changes in the overall shape and form of the protein and its binding pocket, thus providing more information about the system while confirming docking results.

The RMSD of the protein-ligand systems was examined in a similar manner to the apo RdRp to determine whether the simulated system was fit for further analysis and to analyze the stability of the RdRp-ligand complex. When a system has maintained a consistent RMSD over a long duration, the simulation can be accepted as a good estimation of experimental binding. An RMSD value lower than that of the apo protein structure may indicate that the protein-ligand complexes simulated were more stable than the free RdRp complex structure [39]. A shift to a more stable and less dynamic complex suggests the potency of a compound as a potential inhibitor [40].

The representative VIT-, VIX-, and CAN-RdRp complexes had mean RMSDs of 3.0, 2.8, and 2.9 Å, respectively, and all converged before 50 ns for all triplicate production runs. Ultimately, all three complexes involving the hit compounds had a lower mean RMSD value than the apo RdRp structure, indicating greater stability in the three docked systems over the free protein (Figure 4a, Supplementary Figure S3a,b). A comparison between the RMSF plots of free and bound protein structures can identify highly mobile residues and the subsequent changes in dynamics due to ligand interaction. The RMSF values of the nsp12 monomer for the VIT-bound RdRp complex ranged from 0.05 to 0.68 nm, while those for the VIX complex varied between 0.05 and 0.63 nm. On the other hand, RMSF values for CAN were found from 0.05 to 0.66 nm (Figure 4b, Supplementary Figure S4a,b).

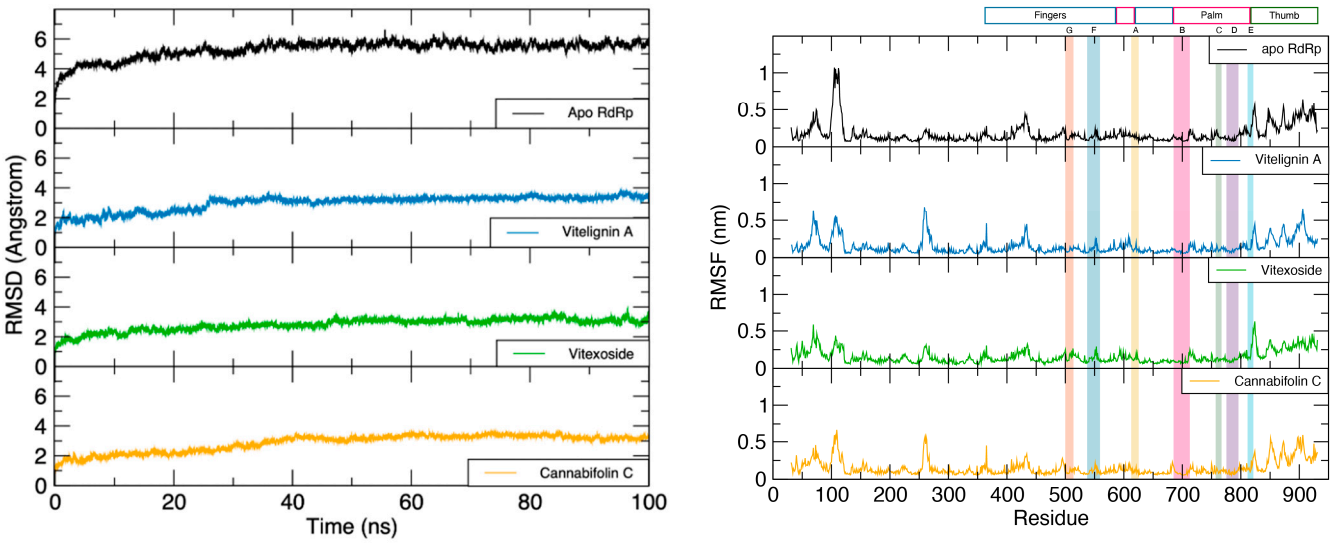

Figure 4. Representative Trajectory Analysis of Natural Product Compound-RdRp Complexes. (**a**) RMSD and (**b**) RMSF plots of the nsp 12 unit for the production run of the apo RdRp complex, VIT-RdRp complex, VIX-RdRp complex, and CAN-RdRp complex. Colored bars highlight residues included in catalytic motifs A–G.

Interestingly, both VIT and CAN natural product compound-bound complexes generally showed decreased RMSF values in residues D100 to T120 for all MD trials, while

VIX displayed a unique increase in flexibility in this region (Supplementary Figure S4a) in comparison to the apo RdRp in one of the MD trials, despite compounds not having direct interactions in this region. It should be noted that among all three candidates, VIT showed the most consistent result, which shows increased rigidity in this region. These residues compose a loop region in the NiRAN domain of RdRp, which, while still a relatively flexible region overall, was found to be more rigid in the VIT- and CAN-bound RdRp complexes compared to the apo structure (Figure 5a–c). Though their exact functional correspondence cannot be elucidated in this study, this shift is notable due to the known significance of loop structures in enzyme active sites and ligand binding sites [41]. Moreover, the NiRAN domain has been reported to mediate NMPylation, RNAylation, and mRNA capping activities at the nsp9 N-terminus. Because this region mediates a wide variety of reactions and is critical for viral replication [42–45], this shift in flexibility would be interesting to examine further.

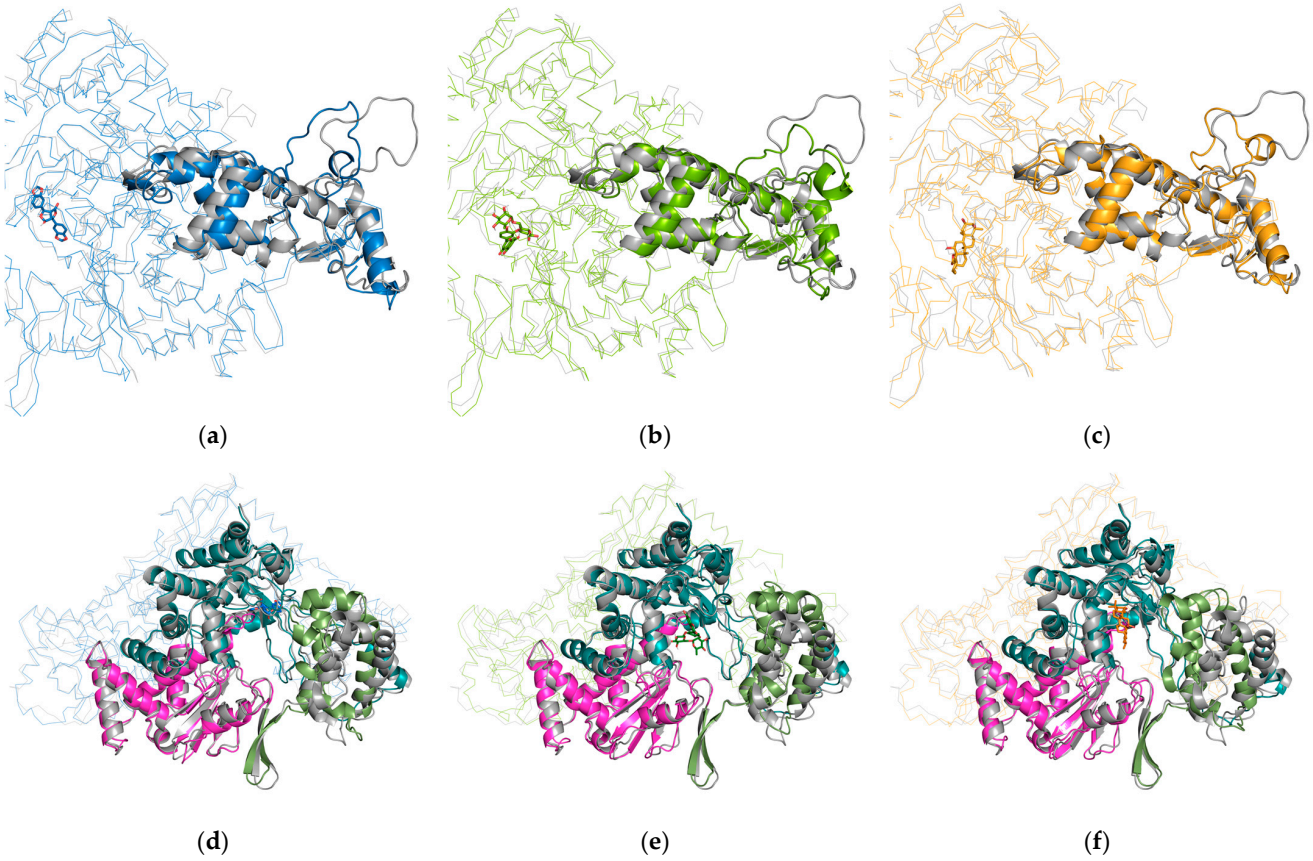

Figure 5. Representative aligned structures of the Natural Product Compound-RdRp Complex with the Clustered Apo RdRp Complex Structure (gray). The NiRAN domain (cartoon representation) of (**a**) Vitelignin A (blue), (**b**) Vitexoside (green), and (**c**) Cannabifolin C (orange). The RNA-binding channel with finger, palm, and thumb subdomains is colored cyan, pink, and pale green, respectively, of (**d**) Vitelignin A, (**e**) Vitexoside, and (**f**) Cannabifolin C.

Additional inspection of the final frames of the ligand-bound production runs in comparison to the MD clustered apo RdRp complex structure exhibited significant structural differences in the retained structures. A noticeable shift in the beta-loop region connecting the palm and thumb domains was noted for the VIT-bound complex compared to the apo RdRp structure. Furthermore, motif E (H810–K821) was observed to behave like a hinge for the RdRp thumb subdomain in all three ligand-bound structures. This resulted in this region shifting closer towards the protein body, which can be posited as the thumb domain trying to close around the bound ligand and stabilize its binding. This is consistent

with a previous report postulating that SARS-CoV RdRp motif E, a conserved region in SARS-CoV-2, controls flexibility in the thumb subdomain [46] (Figure 5d–f). The resulting narrowing of the binding region can also prevent the binding of its natural partner, potentially inhibiting the intended action of RdRp in viral replication.

RdRp in simulations involving both the VIT and CAN complexes was also found to have increased protein flexibility in residues S255 to L270, which constituted another loop structure in the interface connecting the NiRAN and catalytic domains. Additionally, residues V495, N496, N497, and K500 in the VIT-bound RdRp structure were noted to be a part of a region that exhibited a slightly increased rigidity compared to the unbound structure. These residues are observed to interact with the ligand in the obtained clustered structure, suggesting that they may primarily serve as stabilizing interactions for VIT binding. Notably, the residues comprising the thumb subdomain of the catalytic domain of RdRp were also found to exhibit decreased overall flexibility in the VIX-RdRp complex, an observation that may be attributed to the RdRp achieving a stable conformation earlier during the simulation. As previously mentioned, the thumb subdomain has been reported to support the template and primer strands of RNA during replication [1]. Besides competitively inhibiting the active-site domain, a decrease in the flexibility of the palm subdomain may also reduce its adaptability to the changes required for RNA binding and RdRp activity.

Overall, the catalytic domain of VIT-, VIX-, and CAN-bound nsp12 retained its rigid structure, like that of the apo protein structure, especially in the seven catalytic motifs A-G. The decrease in flexibility in parts of the nsp12 may suggest stable binding with the ligands, and that when the ligands are bound to the protein, higher energies will be needed to unbind the compounds and adopt the needed conformation for catalytic activity [47].

3.5. Protein-Ligand Complex Interaction Analysis

Analysis of protein-ligand interactions after MD and clustering showed hydrogen bond interactions between VIT and residues N496, N497, S501, G559, V560, and R569. Hydrophobic interactions were also observed with residues V495, K500, V560, R569, and A685 while van der Waals interactions were found with I494, N543, A558, T565, G683, and D684 (Figure 6a,b, Supplementary Figure S5a,b). Among these, VIT maintained consistent hydrogen bond and hydrophobic interactions with residues V495, N496, R569, and A685 across three separate MD production runs. Overall, an increase in hydrogen bonds and hydrophobic interactions was noted in the clustered structure obtained after 100 ns of simulated movement, suggesting increased stability of VIT binding (Table 3). Hydrogen bonds mediate key interactions between protein and ligand, influencing the binding affinity of a compound to its receptor. Thus, a greater number of hydrogen bonds may indicate stronger binding [48]. Most residues observed in the clustered protein-VIT interaction diagram are typically involved in RNA interactions with the protein, particularly in stabilization and positioning.

Further analysis of VIT through MD and RMSF analysis revealed that the ligand was most flexible in the C11-C12 and C18-C19 regions of the ligand backbone, both pairs being homologous to each other and forming pi-alkyl interactions with binding site residues (Supplementary Figure S6a). Additionally, the RMSF plot showed that atoms O3 and O5 were also relatively flexible and featured similar peaks. These atoms once again composed homologous features in VIT and both participated in alkyl and hydrophobic interactions in the binding site. As observed in the MD production run (Supplementary Figure S6b), the compound was relatively stable within its position in the active-site channel. VIT maintained its position in the tunnel throughout the simulation despite flipping by 90 ns.

This change may explain the higher fluctuations observed for atoms C11, C12, C18, C19, O3, and O5.

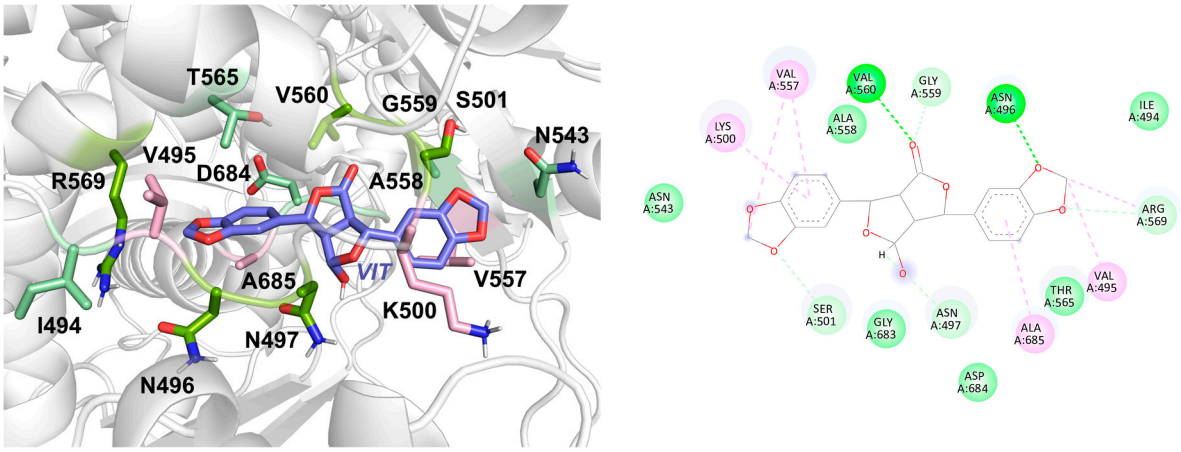

(**a**) (**b**)

Figure 6. Representative post-MD interaction diagrams of VIT-bound to RdRp in (**a**) 3D and (**b**) 2D representation. Residues in (**a**) are highlighted with colors corresponding to the interactions shown in the 2D interaction diagram in (**b**). Hydrogen bonding is displayed as green dashed lines, van der Waals interactions are shown as green circles, and alkyl interactions are shown as pink circles. Blue shadows on the ligand and residues indicate solvent accessibility.

Table 3. Summary of interactions observed for the top 3 compound-RdRp representative complexes after molecular dynamics simulations.

Ligand	Hydrogen Bond	Hydrophobic	Charged	van der Waals
VIT	N496, N497, S501, G559, V560, R569	V495, K500, V560, R569 [1], A685	-	I494, N543, A558, T565, G683, D684
VIX	N496, R555, T556, R569, S681, S682, D684, T687	A685	-	I494, V495, N497, K545, R553, R555, V557, T565, T680, G683, A688, N691, S759
CAN	T565, Q573, D684	R569, H572, A580, A685, T689, T925	-	V560, S564, N568, L576, K577, G590, T686

[1] multiple interactions recorded.

In addition to the number of hydrogen bonds present throughout the simulation, identifying hydrogen bonds between ligand and protein residues is another factor to consider when examining these interactions. When a hydrogen bond interaction between a residue and the ligand is observed for a larger percentage of the simulation, it may be considered relatively more stable. Hydrogen bond analysis of the MD trajectory found that the most frequent hydrogen bonds were with residues N496, V560, and S501, occurring at 28.58%, 12.16%, and 4.12%, respectively. Atoms O3 and O6 were among those involved in the aforementioned hydrogen bonds. These atoms were found to be relatively more flexible and may have allowed the ligand to orient itself to achieve more favorable bonding throughout the simulation.

In the case of VIX, hydrogen bonds were found with residues N496, R555, T556, R569, S681, S682, D684, and T687. Hydrophobic contacts were established with A685 while van der Waals interactions were noted with I494, V495, N497, K545, R553, R555, V557, T565, T680, G683, A688, N691, and S759 (Table 3). Among the RdRp residues, I494, V495, N496, R569, S682, A685, T687, and A688 consistently maintained interactions with VIT across

three independent MD runs. Unfavorable interactions from the docked structure were resolved during the simulation, and none were observed in the final clustered structure (Figure 7a,b, Supplementary Figure S5c,d).

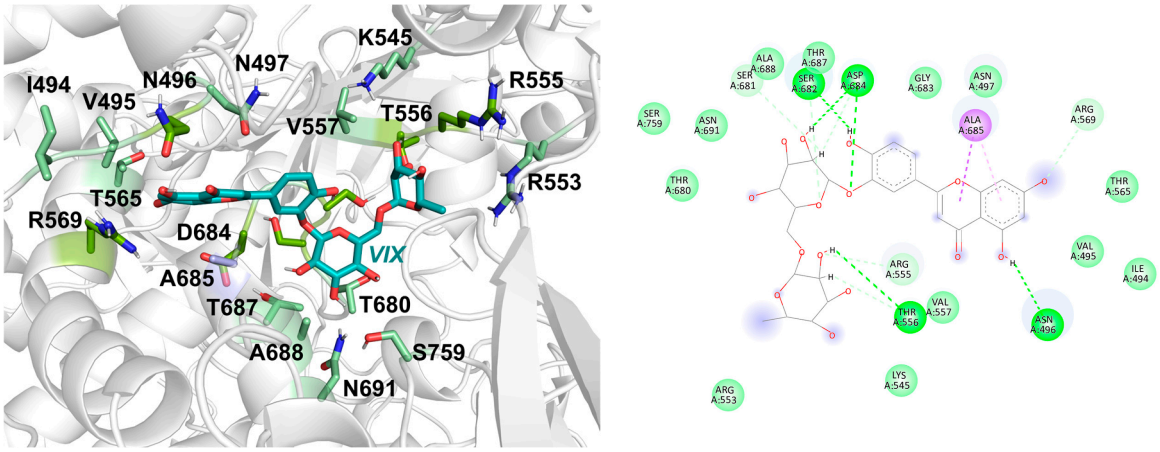

(**a**) (**b**)

Figure 7. Representative post-MD interaction diagrams of VIX-bound to RdRp in (**a**) 3D and (**b**) 2D representation. Residues in (**a**) are highlighted with colors corresponding to the interactions shown in the 2D interaction diagram in (**b**). Hydrogen bonding is displayed as green dashed lines, van der Waals interactions are shown as green circles, and the pi-sigma interactions are shown as a violet circle. Blue shadows on the ligand and residues indicate solvent accessibility.

Among the residues with notable interactions in the clustered structure, S759 was previously noted to be part of the SDD catalytic motif, which is essential for coordinating Mg^{+} ions to the catalytic center in anticipation of NTP addition [49] while residues K545, R553, and R555 were previously noted to be involved in the formation of the NTP entry channel [1]. Residue N691 was also reported to contribute to RNA specificity of the SARS-CoV-2 RdRp [22]. Other residues interacting with the VIX ligand in the clustered structure were also noted to be involved in interactions with RNA.

VIX was noted to have the most prevalent hydrogen bonds with residues D684, T556, and N496, with occupancies of 56.38%, 35.71%, and 32.92% throughout the simulation, respectively. Between the docked and clustered structures, the increase in hydrogen bond interactions with the protein indicates greater binding stability to the protein with respect to the new conformation. These observed interactions may be involved in the formation of more favorable contacts between the protein and ligand during the MD simulation, especially given the relatively frequent occupancy of these bonds. This may have allowed VIX to retain its position within the protein channel more favorably than previously predicted through docking.

RMSF analysis from the MD run elaborated on the dynamics of the ligand in the active-site tunnel during the 100 ns simulation (Supplementary Figure S7a). It was observed that the ligand was highly flexible, as indicated by the markedly fluctuating RMSF values. These fluctuations may have been due to sigma bonds connecting the ringed portions of the ligand, which are able to rotate freely, allowing the compound to change conformation to find a favorable pose around the active site. A large conformational change was observed from the beginning of the simulation to the 20 ns mark (Supplementary Figure S7b). By the 30 ns mark of the simulation, the ligand stabilized in its position and maintained the same relative conformation for the remainder of the simulation.

Across three replicates of the CAN-RdRp system MD simulation, a few overlapping residues were observed to interact with CAN. Despite this, CAN maintained interactions with various reported RdRp RNA interaction sites and active-site residues [9,21,22]. Fur-

thermore, CAN remained stably associated with RdRp throughout the 100 ns simulation. In a representative trial, CAN was observed to establish hydrogen with RdRp residues T565, Q573, and D684, while van der Waals interactions were observed with V560, S564, N568, L576, K577, G590, and T686. New hydrophobic contacts were also recorded with residues R569, H572, A580, A685, T689, and T925 (Table 3; Figure 8a,b, Supplementary Figure S5e,f).

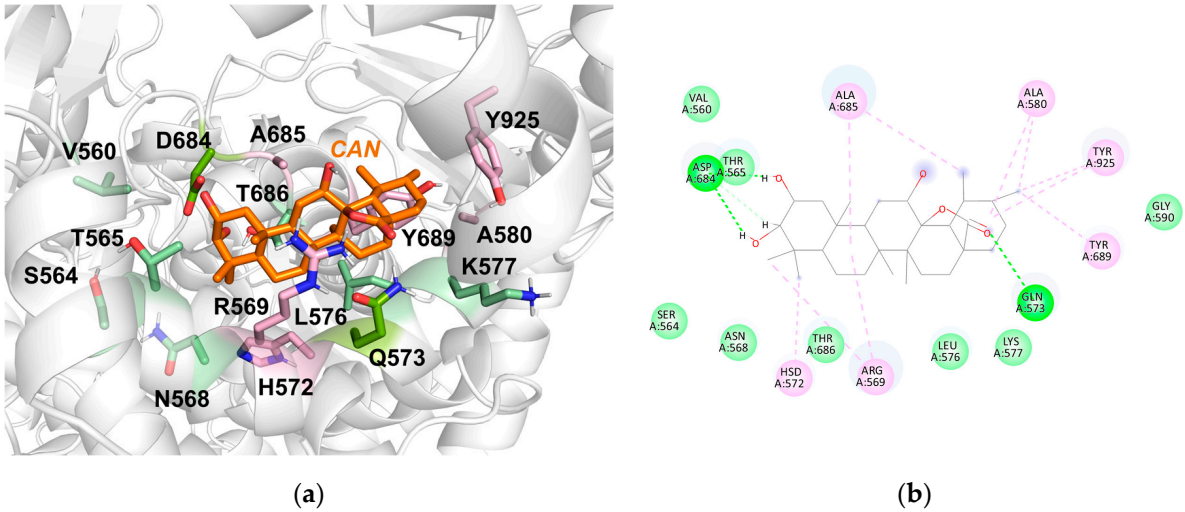

(**a**) (**b**)

Figure 8. Representative post-MD interaction diagrams of CAN-bound to RdRp in (**a**) 3D and (**b**) 2D representation. Residues in (**a**) are highlighted with colors corresponding to the interactions shown in the 2D interaction diagram in (**b**). Hydrogen bonding is displayed as green dashed lines, van der Waals interactions are shown as green circles, and alkyl interactions are shown as pink circles. Blue shadows on the ligand and residues indicate solvent accessibility.

In the docked structure, interactions were observed with S759, D760, and D761 of the RdRp. These were previously noted to complete a catalytic motif conserved in various RdRp proteins that aids in the lengthening of the synthesized RNA strand by coordinating magnesium ions at the catalytic center [1,21]. These interactions were not retained in the post-production clustered structure due to the translocation of the CAN from one side of the active-site channel to another. Hydrogen bond analysis identified bonding with D684, an RNA interaction site residue, at a frequency of 43.39%. This prominent hydrogen bond helped anchor the ligand to its present binding site. The increase in hydrophobic contacts in the final clustered structure also suggests that CAN, a largely hydrophobic molecule, was able to establish contacts with a hydrophobic cavity in the protein channel during the MD simulation, contributing to better binding. Thus, the presence of the ligand in this pocket within the active-site channel may aid in obstructing RNA strand binding and interactions within RdRp.

Among the three ligands, CAN was the most rigid throughout the simulation. The ligand backbone had a low RMSF, with only the hydrogen atoms in the structure showing higher RMSF values and thus higher flexibility (Supplementary Figure S8a). This was expected due to the multi-ringed structure of the compound, which greatly limits the conformations CAN can adapt to over time. Despite this overall rigidity in structure, the molecule adapted by moving around the active site-channel of RdRp frequently during the 100 ns MD simulation (Supplementary Figure S8b). The ligand was observed to have settled in a new position by the 40 ns mark and remained in that conformation until the end of the production run. This indicated that the conformation could possibly be entropically favorable within the active- site channel.

4. Discussion

In this study, a VS approach was utilized to identify the top three potential RdRp inhibitors from a library of 1516 Philippine Natural Product compounds. VIT, VIX, and CAN exhibited better binding affinities to RdRp than RTP, the active form of Remdesivir, an established anti-viral drug [50,51]. Further analysis after docking revealed that all three compounds established interactions with key residues within the RdRp active site. To verify the potential of these compounds to serve as effective RdRp inhibitors, MD simulations were performed, showing that all three compounds remained stably bound to the RdRp active-site region. The introduction of these ligands also resulted in decreased flexibility in the NiRAN domain and movement of the thumb subdomain towards the RNA-binding pocket, revealing two potential inhibitory mechanisms by which these compounds can act on RdRp.

VIT is a furanofuran lignan isolated from the seeds of *Vitex negundo*. The raw material from which the compound is derived has previously been utilized in traditional therapeutics for its anti-inflammatory, analgesic, antioxidant, and antifungal properties [52–56]. Through ADME analysis, the compound was predicted to have a logP of 2.70, which implies favorable oral bioavailability and enough room for drug optimization should it be needed later. For pharmacokinetic properties, VIT was found to have high gastrointestinal (GI) absorption and predicted to be unable to permeate the Blood-Brain-Barrier (BBB). High GI absorption is favorable for oral drug candidates, while the inability to permeate the BBB prevents potential neurotoxicity caused by the molecule when it enters the cell [57]. Additionally, the compound was not found to be a substrate of P-gp, which potentially allows it to have better distribution in the body. Finally, among the CYPs that were analyzed through SwissADME, VIT was found to be an inhibitor for CYP2D6 but not for CYP1A2, CYP2C19, CYP2C9, and CYP3A4. Compounds have differing propensities for CYP inhibition; thus, it is important to assess this characteristic to help predict potential drug–drug interactions. This in silico assessment suggests that precautions must then be taken if VIT is taken concurrently with other drugs to ensure no adverse effects occur when various drugs are in the body. Despite this, the compound notably passed all five in silico drug-likeness filters examined, emphasizing its overall potential to be an orally administered drug.

VIX is a flavonoid glycoside that has previously been isolated from the roots of *Vitex negundo* [36,58]. The compound was predicted to have a logP of 3.26. Additionally, while BBB permeability and CYP inhibition were not observed for VIX, it exhibited low GI absorption and did not act as a P-gp substrate. These properties predict that the overall distribution of the compound within the body may not be as favorable as VIT, and lessens its potential to be developed later on as an oral therapeutic; however, this may potentially be overcome through drug delivery systems or alternative routes of administration.

CAN is a polyoxygenated triterpenoid derived from the leaves of *Vitex negundo*, first isolated from the cannabifolia variety of the species. The same study that reported this compound also suggested that it, along with the other triterpenoids from the plant, could be partially responsible for the anti-inflammatory responses observed in the traditional uses of Vitex plants [33]. ADME analysis showed that this compound had the highest logP value among the three hit compounds examined at 3.60, indicating that it is relatively less water-soluble than the prior two ligands. Despite this, its oral bioavailability score still falls within an acceptable range, with GI absorption projected to be high. The compound was found to be a P-gp substrate, but it was predicted to have low BBB permeability and was not found to inhibit cytochrome P450 enzymes.

Each of the top compounds was predicted to have promising ADME profiles, with VIT showing the best drug-like features due to its favorable oral bioavailability and high

GI absorption. Furthermore, its predicted logP value shows that VIT is a strong candidate for further lead optimization to improve its efficacy. Taken together, the three compounds have a high potential to be developed into an anti-COVID-19 treatment. Since the RdRp active site is highly conserved among RNA viruses, these compounds may also function as broad-spectrum antivirals.

Notably, all three can be sourced from various parts of *Vitex negundo*, a plant native to the Philippines. Lagundi, as it is known locally, has been studied extensively in the Philippines for its therapeutic capabilities and is currently approved for use medicinally, particularly against cough, asthma, and other respiratory ailments [59]. Natural product compounds from this plant have been known for their anti-histamine, anti-inflammatory, and antioxidant properties, among others [37]. These characteristics make it a promising treatment for COVID-19, a respiratory disease associated with pulmonary inflammation [60]. The local availability of *Vitex negundo* and its previously documented functions make VIT, VIX, and CAN, along with other natural products derived from various parts of the *Vitex negundo* plant, an attractive source of compounds to further examine for COVID-19 treatment.

5. Conclusions

SARS-CoV-2 RNA-dependent RNA polymerase is an enzyme that plays a vital role in the viral life cycle, making it an attractive target for potential COVID-19 therapeutics. Previous computational studies have examined databases of approved drugs and regional natural products in the effort to identify compounds that may inhibit SARS-CoV-2 RdRp. Natural products have been liberally used in traditional medicine to treat a variety of ailments and have been known to possess favorable properties that mediate inflammation and a variety of infections, among others. These properties make natural compounds a rich pool of molecules to examine in drug discovery.

This study contributes to the search for potential inhibitory compounds against SARS-CoV-2 by examining a library of Philippine Natural Products against RdRp using in silico compound screening and validation. Through MD, the behavior of SARS-CoV-2 RNA-dependent RNA-polymerase in complex with its cofactors nsp7 and nsp8 was simulated in physiological conditions. The catalytic domain of apo RdRp was observed to be relatively stable, especially in the regions of motifs A-G, while regions of high flexibility were identified in the C-terminal NiRAN domain and N-terminal thumb subdomain. The overall stability of the complex provided an optimized structure at physiological conditions that was used to examine protein-ligand interactions through docking.

High-throughput virtual screening of the Philippine Natural Products library resulted in the identification of three compounds previously isolated from the *Vitex negundo* plant, VIT, VIX, and CAN, as potential candidates for RdRp inhibition. Further studies through MD, which examined the interactions between compound hits identified in virtual screening and the RdRp functional unit, verified the relative stability of all three protein-ligand complexes in a dynamic environment when compared to the apo-protein complex.

Referencing the high binding affinities and interactions to the protein, favorable predictions in ADME properties, and their stability in a dynamic environment, the three hit compounds were found to be the best candidates for further examination and work using in vitro viral assays. VIT, VIX, and CAN were found to be previously unstudied for SARS-CoV-2 inhibition, all of which come from a commonly available Philippine medicinal plant, *Vitex negundo*. Its current medicinal application in the Philippines, especially for respiratory ailments, increases its appeal as a therapeutic.

Overall, the results of this study provide relevant information on potential therapeutic candidates that can be obtained from local plants and can be used to target SARS-

CoV-2 RdRp with the help of computational methods, though experimental validation through in vitro or in vivo techniques and further structural optimization are needed to assess all three candidates' efficacy against the intended target as well as improve their properties, respectively.

Supplementary Materials: The following supporting information can be downloaded at: https://www.mdpi.com/article/10.3390/covid6070129/s1, Figure S1: Overlaid nsp12 structure of the crystal RdRp complex structure (grey) obtained from the CHARMM-GUI Archive and the representative structure of the most populated cluster of apo RdRp complex (magenta) after MD simulation; Figure S2: 2D Protein-Ligand Interactions Diagrams for (a) isocannabilignin, (b) cannabilignin, (c) vitexnegheteroin I, (d) vitelignin A, (e) vitegnoside, (f) vitexoside, (g) sesamolinol 4′-O-β-D-glucosyl-(1-6)-O-β-D-glucoside, (h) 6-(p-hydroxybenzoyl)mussaenosidic acid, (i) cannabifolin C, and (j) guadial C; Figure S3: RMSD Analysis of MD production run (a) trial 2 and (b) trial 3; Figure S4: RMSF Analysis of MD production run (a) trial 2 and (b) trial 3; Figure S5: Post-MD interaction diagrams of VIT (a) trial 2 and (b) trial 3, VIX (c) trial 2 and (d) trial 3, and CAN (e) trial 2 and (f) trial 3; Figure S6: Trajectory analysis of VIT binding; Figure S7: Trajectory analysis of VIX binding; Figure S8: Trajectory analysis of CAN binding. Table S1: Top 25% of Philippine Natural Product Compounds above the control cutoff (RTP, -7.9 kcal/mol) sorted based on PAINS Alert score, Predicted Affinity, Lipophilicity, and Synthetic Accessibility; Table S2: 2D structures and binding Affinities for the Best Docked Pose of the Top 10 Philippine Natural Product Compounds Based on ADME screening and Protein-Ligand Interactions; Table S3: Predicted ADME profiles of Top 10 Hit Compounds.

Author Contributions: Conceptualization, S.J.Y.M., J.B.B., L.A.E.M. and M.C.O.C.; methodology, A.I.D.A. and S.J.Y.M.; validation, A.I.D.A., S.J.Y.M. and M.C.O.C.; formal analysis, A.I.D.A.; investigation, A.I.D.A., S.J.Y.M. and M.C.O.C.; data curation, A.I.D.A. and S.J.Y.M.; writing—original draft preparation, A.I.D.A., A.P.L., S.J.Y.M. and M.C.O.C.; writing—review and editing, A.I.D.A., A.P.L., J.B.B., L.A.E.M., S.J.Y.M. and M.C.O.C.; supervision, S.J.Y.M. and M.C.O.C.; project administration, J.B.B., L.A.E.M., S.J.Y.M. and M.C.O.C.; funding acquisition, M.C.O.C. All authors have read and agreed to the published version of the manuscript.

Funding: This work was supported by a Philippine Council for Health Research and Development (PCHRD) grant (DV No. 2022-0306-10) to S.J.Y.M., J.B.B., L.A.E.M. and M.C.O.C.

Institutional Review Board Statement: Not applicable.

Informed Consent Statement: Not applicable.

Data Availability Statement: The datasets generated and/or analyzed during the current study are available in the manuscript and Supplementary Materials.

Acknowledgments: During the preparation of this study, the authors used the Computing and Archiving Research Environment (COARE) High-Performance Computing facilities for the purposes of executing molecular dynamics simulations. The authors have reviewed and edited the output and take full responsibility for the content of this publication.

Conflicts of Interest: The authors declare no conflicts of interest.

Abbreviations

The following abbreviations are used in this manuscript:

RdRp	RNA-dependent RNA-polymerase
SARS-CoV-2	Severe Acute Respiratory Syndrome Coronavirus 2
COVID-19	Coronavirus disease 19
VS	Virtual screening
ADME	Absorption, Distribution, Metabolism, and Excretion
VIT	Vitelignin A
VIX	Vitexoside

CAN	Cannabifolin C
MD	Molecular dynamics
S	Spike
E	Envelope
M	Membrane
N	Nucleocapsid
nsp	nonstructural proteins
NTP	Nucleoside triphosphates
RCSB PDB	Research Collaboratory for Structural Bioinformatics Protein Data Bank
PME	Particle Mesh Ewald
LINCS	LINear Constraint Solver
RMSD	Root Mean Square Deviation
RMSF	Root Mean Square Fluctuation
ROG	Radius of Gyration
RTP	Remdesivir Triphosphate
MMFF94	Merck Molecular Force Field 94
NiRAN	Nidovirus RdRp-Associated Nucleotidyl transferase
PAINS	Pan-Assay Interference Compounds
GI	gastrointestinal
BBB	Blood-Brain-Barrier

References

1. Gao, Y.; Yan, L.; Huang, Y.; Liu, F.; Zhao, Y.; Cao, L.; Wang, T.; Sun, Q.; Ming, Z.; Zhang, L.; et al. Structure of the RNA-Dependent RNA Polymerase from COVID-19 Virus. *Science* **2020**, *368*, 779–782. [CrossRef] [PubMed]
2. Lu, H.; Stratton, C.W.; Tang, Y. Outbreak of Pneumonia of Unknown Etiology in Wuhan, China: The Mystery and the Miracle. *J. Med. Virol.* **2020**, *92*, 401–402. [CrossRef] [PubMed]
3. Wu, F.; Zhao, S.; Yu, B.; Chen, Y.-M.; Wang, W.; Song, Z.-G.; Hu, Y.; Tao, Z.-W.; Tian, J.-H.; Pei, Y.-Y.; et al. A New Coronavirus Associated with Human Respiratory Disease in China. *Nature* **2020**, *579*, 265–269. [CrossRef] [PubMed]
4. World Health Organization. COVID-19 Cases | WHO COVID-19. Dashboard. Available online: https://data.who.int/dashboards/covid19/cases (accessed on 27 December 2025).
5. Shereen, M.A.; Khan, S.; Kazmi, A.; Bashir, N.; Siddique, R. COVID-19 Infection: Emergence, Transmission, and Characteristics of Human Coronaviruses. *J. Adv. Res.* **2020**, *24*, 91–98. [CrossRef] [PubMed]
6. Lai, C.-C.; Shih, T.-P.; Ko, W.-C.; Tang, H.-J.; Hsueh, P.-R. Severe Acute Respiratory Syndrome Coronavirus 2 (SARS-CoV-2) and Coronavirus Disease-2019 (COVID-19): The Epidemic and the Challenges. *Int. J. Antimicrob. Agents* **2020**, *55*, 105924. [CrossRef] [PubMed]
7. Wu, C.; Liu, Y.; Yang, Y.; Zhang, P.; Zhong, W.; Wang, Y.; Wang, Q.; Xu, Y.; Li, M.; Li, X.; et al. Analysis of Therapeutic Targets for SARS-CoV-2 and Discovery of Potential Drugs by Computational Methods. *Acta Pharm. Sin. B* **2020**, *10*, 766–788. [CrossRef] [PubMed]
8. McDonald, S.M. RNA Synthetic Mechanisms Employed by Diverse Families of RNA Viruses. *WIREs RNA* **2013**, *4*, 351–367. [CrossRef] [PubMed]
9. Aftab, S.O.; Ghouri, M.Z.; Masood, M.U.; Haider, Z.; Khan, Z.; Ahmad, A.; Munawar, N. Analysis of SARS-CoV-2 RNA-Dependent RNA Polymerase as a Potential Therapeutic Drug Target Using a Computational Approach. *J. Transl. Med.* **2020**, *18*, 275. [CrossRef] [PubMed]
10. Jo, S.; Kim, T.; Iyer, V.G.; Im, W. CHARMM-GUI: A Web-based Graphical User Interface for CHARMM. *J. Comput. Chem.* **2008**, *29*, 1859–1865. [CrossRef] [PubMed]
11. Abraham, M.J.; Murtola, T.; Schulz, R.; Páll, S.; Smith, J.C.; Hess, B.; Lindahl, E. GROMACS: High Performance Molecular Simulations through Multi-Level Parallelism from Laptops to Supercomputers. *SoftwareX* **2015**, *1–2*, 19–25. [CrossRef]
12. Pronk, S.; Páll, S.; Schulz, R.; Larsson, P.; Bjelkmar, P.; Apostolov, R.; Shirts, M.R.; Smith, J.C.; Kasson, P.M.; Van Der Spoel, D.; et al. GROMACS 4.5: A High-Throughput and Highly Parallel Open Source Molecular Simulation Toolkit. *Bioinformatics* **2013**, *29*, 845–854. [CrossRef] [PubMed]
13. Bjelkmar, P.; Larsson, P.; Cuendet, M.A.; Hess, B.; Lindahl, E. Implementation of the CHARMM Force Field in GROMACS: Analysis of Protein Stability Effects from Correction Maps, Virtual Interaction Sites, and Water Models. *J. Chem. Theory Comput.* **2010**, *6*, 459–466. [CrossRef] [PubMed]
14. Nosé, S. A Molecular Dynamics Method for Simulations in the Canonical Ensemble. *Mol. Phys.* **1984**, *52*, 255–268. [CrossRef]

15. Hoover, W.G. Canonical Dynamics: Equilibrium Phase-Space Distributions. *Phys. Rev. A* **1985**, *31*, 1695–1697. [CrossRef] [PubMed]
16. Parrinello, M.; Rahman, A. Polymorphic Transitions in Single Crystals: A New Molecular Dynamics Method. *J. Appl. Phys.* **1981**, *52*, 7182–7190. [CrossRef]
17. O'Boyle, N.M.; Banck, M.; James, C.A.; Morley, C.; Vandermeersch, T.; Hutchison, G.R. Open Babel: An Open Chemical Toolbox. *J. Cheminform.* **2011**, *3*, 33. [CrossRef] [PubMed]
18. Morris, G.M.; Huey, R.; Lindstrom, W.; Sanner, M.F.; Belew, R.K.; Goodsell, D.S.; Olson, A.J. AutoDock4 and AutoDockTools4: Automated Docking with Selective Receptor Flexibility. *J. Comput. Chem.* **2009**, *30*, 2785–2791. [CrossRef] [PubMed]
19. Sanner, M.F. Python: A Programming Language for Software Integration and Development. *J. Mol. Graph. Model.* **1999**, *17*, 57–61. [PubMed]
20. Trott, O.; Olson, A.J. AutoDock Vina: Improving the Speed and Accuracy of Docking with a New Scoring Function, Efficient Optimization, and Multithreading. *J. Comput. Chem.* **2010**, *31*, 455–461. [CrossRef] [PubMed]
21. Yin, W.; Mao, C.; Luan, X.; Shen, D.-D.; Shen, Q.; Su, H.; Wang, X.; Zhou, F.; Zhao, W.; Gao, M.; et al. Structural Basis for Inhibition of the RNA-Dependent RNA Polymerase from SARS-CoV-2 by Remdesivir. *Science* **2020**, *368*, 1499–1504. [CrossRef] [PubMed]
22. Hillen, H.S.; Kokic, G.; Farnung, L.; Dienemann, C.; Tegunov, D.; Cramer, P. Structure of Replicating SARS-CoV-2 Polymerase. *Nature* **2020**, *584*, 154–156. [CrossRef] [PubMed]
23. Schrödinger, LLC PyMOL. Available online: https://www.pymol.org/ (accessed on 27 December 2025).
24. Daina, A.; Michielin, O.; Zoete, V. SwissADME: A Free Web Tool to Evaluate Pharmacokinetics, Drug-Likeness and Medicinal Chemistry Friendliness of Small Molecules. *Sci. Rep.* **2017**, *7*, 42717. [CrossRef] [PubMed]
25. BIOVIA Dassault Systèmes BIOVIA. Available online: https://www.3ds.com/products/biovia/discovery-studio/visualization (accessed on 27 December 2025).
26. Hanwell, M.D.; Curtis, D.E.; Lonie, D.C.; Vandermeersch, T.; Zurek, E.; Hutchison, G.R. Avogadro: An Advanced Semantic Chemical Editor, Visualization, and Analysis Platform. *J. Cheminform.* **2012**, *4*, 17. [CrossRef] [PubMed]
27. Zoete, V.; Cuendet, M.A.; Grosdidier, A.; Michielin, O. SwissParam: A Fast Force Field Generation Tool for Small Organic Molecules. *J. Comput. Chem.* **2011**, *32*, 2359–2368. [CrossRef] [PubMed]
28. Humphrey, W.; Dalke, A.; Schulten, K. VMD: Visual Molecular Dynamics. *J. Mol. Graph.* **1996**, *14*, 33–38. [CrossRef] [PubMed]
29. Bottegoni, G.; Rocchia, W.; Cavalli, A. Application of Conformational Clustering in Protein–Ligand Docking. In *Computational Drug Discovery and Design*; Baron, R., Ed.; Methods in Molecular Biology; Springer: New York, NY, USA, 2012; Volume 819, pp. 169–186, ISBN 978-1-61779-464-3.
30. Baell, J.B.; Nissink, J.W.M. Seven Year Itch: Pan-Assay Interference Compounds (PAINS) in 2017-Utility and Limitations. *ACS Chem. Biol.* **2018**, *13*, 36–44. [CrossRef] [PubMed]
31. Gautam, L.; Shrestha, S.; Wagle, P.; Tamrakar, B. Chemical Constituents from *Vitex negundo* (Linn.) of Nepalese Origin. *Sci. World* **2010**, *6*, 27–32. [CrossRef]
32. Hu, P.; Li, D.-H.; Jia, C.-C.; Liu, Q.; Wang, X.-F.; Li, Z.-L.; Hua, H.-M. Bioactive Constituents from *Vitex negundo* var. *heterophylla* and Their Antioxidant and α-Glucosidase Inhibitory Activities. *J. Funct. Foods* **2017**, *35*, 236–244. [CrossRef]
33. Li, M.-M.; Su, X.-Q.; Sun, J.; Gu, Y.-F.; Huang, Z.; Zeng, K.-W.; Zhang, Q.; Zhao, Y.-F.; Ferreira, D.; Zjawiony, J.K.; et al. Anti-Inflammatory Ursane- and Oleanane-Type Triterpenoids from *Vitex negundo* var. *cannabifolia*. *J. Nat. Prod.* **2014**, *77*, 2248–2254. [CrossRef] [PubMed]
34. Sehgal, C.K.; Taneja, S.C.; Dhar, K.L.; Atal, C.K. 6′-p-Hydroxybenzoylmussaenosidic Acid-an Iridoid Glucoside from *Vitex negundo*. *Phytochemistry* **1983**, *22*, 1036–1038. [CrossRef]
35. Li, Y.-T.; Li, M.-M.; Sun, J.; Zhu, Z.-X.; Song, Y.-L.; Pang, D.-R.; Zheng, J.; Zhao, Y.-F.; Tu, P.-F.; Li, J. Furofuran Lignan Glucosides from the Leaves of *Vitex negundo* var. *cannabifolia*. *Nat. Prod. Res.* **2017**, *31*, 918–924. [CrossRef] [PubMed]
36. Singh, Y.; Mishra, P.; Kannojia, P. Morphology, Phytochemistry and Pharmacological Activity of *Vitex negundo*: An Overview. *J. Drug Deliv. Ther.* **2020**, *10*, 280–285. [CrossRef]
37. Zheng, C.-J.; Lan, X.-P.; Cheng, R.-B.; Huang, B.-K.; Han, T.; Zhang, Q.-Y.; Zhang, H.; Rahman, K.; Qin, L.-P. Furanofuran Lignans from *Vitex negundo* Seeds. *Phytochem. Lett.* **2011**, *4*, 298–300. [CrossRef]
38. De Vivo, M.; Masetti, M.; Bottegoni, G.; Cavalli, A. Role of Molecular Dynamics and Related Methods in Drug Discovery. *J. Med. Chem.* **2016**, *59*, 4035–4061. [CrossRef] [PubMed]
39. Liu, K.; Watanabe, E.; Kokubo, H. Exploring the Stability of Ligand Binding Modes to Proteins by Molecular Dynamics Simulations. *J. Comput. Aided Mol. Des.* **2017**, *31*, 201–211. [CrossRef] [PubMed]
40. El Hassab, M.A.; Shoun, A.A.; Al-Rashood, S.T.; Al-Warhi, T.; Eldehna, W.M. Identification of a New Potential SARS-CoV-2 RNA-Dependent RNA Polymerase Inhibitor via Combining Fragment-Based Drug Design, Docking, Molecular Dynamics, and MM-PBSA Calculations. *Front. Chem.* **2020**, *8*, 584894. [CrossRef] [PubMed]
41. Lee, C.-Y.; McNerney, C.; Ma, K.; Zhao, W.; Wang, A.; Myong, S. R-Loop Induced G-Quadruplex in Non-Template Promotes Transcription by Successive R-Loop Formation. *Nat. Commun.* **2020**, *11*, 3392. [CrossRef] [PubMed]

42. Slanina, H.; Madhugiri, R.; Bylapudi, G.; Schultheiß, K.; Karl, N.; Gulyaeva, A.; Gorbalenya, A.E.; Linne, U.; Ziebuhr, J. Coronavirus Replication–Transcription Complex: Vital and Selective NMPylation of a Conserved Site in Nsp9 by the NiRAN-RdRp Subunit. *Proc. Natl. Acad. Sci. USA* **2021**, *118*, e2022310118. [CrossRef] [PubMed]
43. Wang, B.; Svetlov, D.; Artsimovitch, I. NMPylation and De-NMPylation of SARS-CoV-2 Nsp9 by the NiRAN Domain. *Nucleic Acids Res.* **2021**, *49*, 8822–8835. [CrossRef] [PubMed]
44. Park, G.J.; Osinski, A.; Hernandez, G.; Eitson, J.L.; Majumdar, A.; Tonelli, M.; Henzler-Wildman, K.; Pawłowski, K.; Chen, Z.; Li, Y.; et al. The Mechanism of RNA Capping by SARS-CoV-2. *Nature* **2022**, *609*, 793–800. [CrossRef] [PubMed]
45. Small, G.I.; Fedorova, O.; Olinares, P.D.B.; Chandanani, J.; Banerjee, A.; Choi, Y.J.; Molina, H.; Chait, B.T.; Darst, S.A.; Campbell, E.A. Structural and Functional Insights into the Enzymatic Plasticity of the SARS-CoV-2 NiRAN Domain. *Mol. Cell* **2023**, *83*, 3921–3930.e7. [CrossRef] [PubMed]
46. Xu, X. Molecular Model of SARS Coronavirus Polymerase: Implications for Biochemical Functions and Drug Design. *Nucleic Acids Res.* **2003**, *31*, 7117–7130. [CrossRef] [PubMed]
47. Teague, S.J. Implications of Protein Flexibility for Drug Discovery. *Nat. Rev. Drug Discov.* **2003**, *2*, 527–541. [CrossRef] [PubMed]
48. Bitencourt-Ferreira, G.; Veit-Acosta, M.; De Azevedo, W.F. Hydrogen Bonds in Protein-Ligand Complexes. In *Docking Screens for Drug Discovery*; De Azevedo, W.F., Ed.; Methods in Molecular Biology; Springer: New York, NY, USA, 2019; Volume 2053, pp. 93–107, ISBN 978-1-4939-9751-0.
49. Jiang, Y.; Yin, W.; Xu, H.E. RNA-Dependent RNA Polymerase: Structure, Mechanism, and Drug Discovery for COVID-19. *Biochem. Biophys. Res. Commun.* **2021**, *538*, 47–53. [CrossRef] [PubMed]
50. Gordon, C.J.; Tchesnokov, E.P.; Woolner, E.; Perry, J.K.; Feng, J.Y.; Porter, D.P.; Götte, M. Remdesivir Is a Direct-Acting Antiviral That Inhibits RNA-Dependent RNA Polymerase from Severe Acute Respiratory Syndrome Coronavirus 2 with High Potency. *J. Biol. Chem.* **2020**, *295*, 6785–6797. [CrossRef] [PubMed]
51. Siegel, D.; Hui, H.C.; Doerffler, E.; Clarke, M.O.; Chun, K.; Zhang, L.; Neville, S.; Carra, E.; Lew, W.; Ross, B.; et al. Discovery and Synthesis of a Phosphoramidate Prodrug of a Pyrrolo[2,1-*f*][Triazin-4-Amino] Adenine *C*-Nucleoside (GS-5734) for the Treatment of Ebola and Emerging Viruses. *J. Med. Chem.* **2017**, *60*, 1648–1661. [CrossRef] [PubMed]
52. Chawla, A.S.; Sharma, A.K.; Handa, S.S.; Dhar, K.L. Chemical Investigation and Anti-Inflammatory Activity of *Vitex negundo* Seeds. *J. Nat. Prod.* **1992**, *55*, 163–167. [CrossRef] [PubMed]
53. Ono, M.; Nishida, Y.; Masuoka, C.; Li, J.-C.; Okawa, M.; Ikeda, T.; Nohara, T. Lignan Derivatives and a Norditerpene from the Seeds of *Vitex negundo*. *J. Nat. Prod.* **2004**, *67*, 2073–2075. [CrossRef] [PubMed]
54. Mahmud, S.; Shareef, H.; Farrukh, U.; Kamil, A.; Rizwani, G.H. Antifungal Activities of *Vitex negundo* Linn. *Pak. J. Bot.* **2009**, *41*, 1941–1943.
55. Zheng, C.-J.; Tang, W.-Z.; Huang, B.-K.; Han, T.; Zhang, Q.-Y.; Zhang, H.; Qin, L.-P. Bioactivity-Guided Fractionation for Analgesic Properties and Constituents of *Vitex negundo* L. Seeds. *Phytomedicine* **2009**, *16*, 560–567. [CrossRef]
56. Zheng, C.-J.; Huang, B.-K.; Wang, Y.; Ye, Q.; Han, T.; Zhang, Q.-Y.; Zhang, H.; Qin, L.-P. Anti-Inflammatory Diterpenes from the Seeds of *Vitex negundo*. *Bioorg. Med. Chem.* **2010**, *18*, 175–181. [CrossRef] [PubMed]
57. Pimentel, E.; Sivalingam, K.; Doke, M.; Samikkannu, T. Effects of Drugs of Abuse on the Blood-Brain Barrier: A Brief Overview. *Front. Neurosci.* **2020**, *14*, 513. [CrossRef] [PubMed]
58. Singh, P.; Mishra, G.; Srivastava, S.; Srivastava, S.; Jha, K.K.; Khosa, R.L. Phytopharmacological Review of *Vitex negundo* (Sambhalu). *Pharmacologyonline* **2011**, *2*, 1355–1385.
59. Alegado-Bagaoisan, D.-M.; Castro, M.C.R.; Purificacion, J.M. A Systematic Review on *Vitex negundo* (NIRPROMP Formulations) for the Treatment of Acute Cough of Mild to Moderate Severity in Pediatric Patients. *Acta Med. Philipp.* **2020**, *54*, 36–43. [CrossRef]
60. Huang, C.; Wang, Y.; Li, X.; Ren, L.; Zhao, J.; Hu, Y.; Zhang, L.; Fan, G.; Xu, J.; Gu, X.; et al. Clinical Features of Patients Infected with 2019 Novel Coronavirus in Wuhan, China. *Lancet* **2020**, *395*, 497–506. [CrossRef] [PubMed]